

We are IntechOpen, the world's leading publisher of Open Access books Built by scientists, for scientists

6,200

Open access books available

169,000

International authors and editors

185M

Downloads

Our authors are among the

154

Countries delivered to

TOP 1%

most cited scientists

12.2%

Contributors from top 500 universities



WEB OF SCIENCE™

Selection of our books indexed in the Book Citation Index
in Web of Science™ Core Collection (BKCI)

Interested in publishing with us?
Contact book.department@intechopen.com

Numbers displayed above are based on latest data collected.
For more information visit www.intechopen.com



Chapter

Ridge Gap Waveguide Beamforming Components and Antennas for Millimeter-Wave Applications

*Mohammad Ali AbdElraheem, Mohamed Mamdouh M. Ali,
Islam Afifi and Abdel R. Sebak*

Abstract

With the improvement of mobile communication technologies and their broad applications, mobile communication will have more impact on our life. Such systems will support a variety of personal communication services with high-data rate and very low latency applications. To achieve such demands, many proposals associated with the development of 5G identify a set of requirements for which different technological directions are independently emerging. One direction is utilizing the millimeter-wave (mm-Wave) frequency bands where more spectrums are available. Millimeter-wave frequencies offer the advantage of physically smaller components that results in cost-effective RF transceivers and feasible large-scale integrated phased arrays. The smart RF transceivers of 5G along with the potential high-frequency innovative designs must satisfy the growing consumer and technology requirements. This implies utilizing the state-of-the-art guiding structures, especially printed ridge gap waveguide (PRGW), that have low loss and minimal dispersion compared with traditional PCB-based structures. The present chapter focuses on the necessary components for a beamforming antenna system which is implemented using PRGW technology. Millimeter wave antennas with different polarizations have been addressed. Power combining and dividing components have been also developed. These components have been used for integration in a complete beamforming antenna system working at an mm-Wave frequency band.

Keywords: millimeter wave, electromagnetic band gap (EBG) structure, printed ridge gap waveguide (PRGW), butler matrix, beam switching

1. Introduction

Wireless technology and devices are fundamental components in many aspects of life including personal communications, internet activities, sensing, and imaging applications for industrial and medical purposes. Wireless technology development is always encouraged by the needs of these applications to enhance their performance in terms of

service quality and cost. A fundamental issue in wireless technology is the system operating frequency which varies according to the target application. An overview of the operating standards in wireless technology reveals that most systems nowadays operate in the microwave frequency band below 3 GHz [1–7]. The current state of wireless applications reflects the demand for using higher frequency bands to enhance the performance of the wireless system. For instance, communication technology is rapidly pushed toward next-generation networks where massive data rates, very low latency, and a high level of service integration are required to enhance the performance of the wireless communication system [8, 9]. To achieve these demands, much higher bandwidths must be used to increase the capacity of the communication channel. Imaging systems are also in the demand of using higher frequencies to overcome the resolution limits at the lower microwave band. Millimeter-Wave frequency range is beyond 30 GHz, where the relative bandwidth is equivalent to multiples of frequency channels at the sub 3 GHz range. Moreover, the signal wavelength at mm-Wave is significantly small and enables high-resolution imaging. These advantages have encouraged the move to the mm-Wave band and have ignited the spark of innovating components with superior characteristics in these high frequencies [10–13].

Many challenges are addressed in the literature, where the small-signal wavelength at the mm-Wave band results in components with small physical dimensions that need high tolerance fabrication facilities with an extremely large cost. In addition, being an advantage that enables integrating large systems in a small area, this is also a limiting property for the power that can be handled by an mm-Wave communications device [14–16]. Hence, antenna arrays must be used in mm-Wave transceivers to provide a suitable amount of gain, especially to compensate for the large path loss caused by atmospheric attenuation at frequencies like 60 GHz and such [17, 18]. Furthermore, the high level of versatility in the next generation network requires running multiple services simultaneously, a property that forces the use of a diversity technique to enable various communications without the need to add bandwidth [19, 20]. Such demand can be realized using multiple-input multiple-output (MIMO) systems employing beamforming techniques to benefit from the deployed high gain array [21, 22]. Therefore, the beamforming antenna array is an essential subject in mm-Wave research in the context of next-generation networks and imaging systems. Several techniques are proposed to implement a beamforming antenna array, which required the usage of various microwave components including power dividers, crossovers, phase shifters, hybrid couplers, and antennas [23–26]. However, the realization of these components at mm-Wave frequencies using traditional printed guiding technologies is another key challenge that needs to be tackled. Although traditional guiding structures such as microstrip line and stripline support a Q-TEM mode, which is subject to minimal dispersion, it has high radiation and dielectric losses at mm-Wave frequencies [27]. On the other hand, a modern guiding structure such as substrate integrated waveguide (SIW) is developed at mm-Wave frequencies as it has low radiation losses compared to microstrip line and stripline structures [28, 29]. However, it can support only TE mode which is subject to large dispersion and causes signal distortion [30, 31]. In addition, the signal is totally propagating inside a dielectric, which leads to high losses at mm-Wave frequencies. Therefore, a novel technology of guiding structures is introduced to provide a solution for the mentioned challenges. This technology is the printed ridge gap waveguide (PRGW) technology that was introduced as a novel low loss Q-TEM guiding structure for the mm-wave frequency range [32–40].

The printed ridge gap structure is shown in **Figure 1a**, where the operating mechanism is based on the idea of wave suppression between a perfect electric conductor

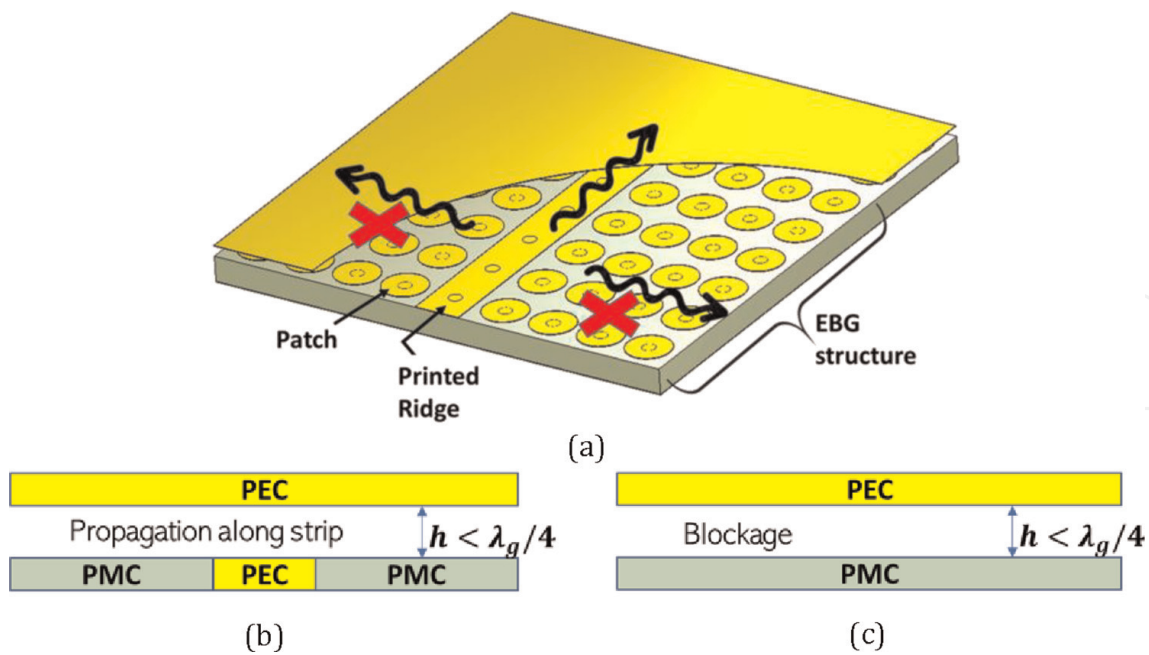


Figure 1. Parallel Plate PEC/PMC structure. (a) PRGW with mushroom EBG cells. (b) achieving propagation with added longitudinal middle strip (c) blockage condition.

(PEC) and a perfect magnetic conductor (PMC) parallel to each other. Such parallel plate structure does not allow wave propagation unless the separation between the plates is enough for achieving zero tangential fields at one plate and zero normal at the other. This cannot happen for separations less than a quarter wavelength. Such condition is used to prevent wave leakage through the sides of the guiding structure, where adding a middle ridge allows having a propagating mode in the longitudinal direction as shown in **Figure 1b**. Since the PMC material does not exist in practice, an emulation of such material is the artificial magnetic conductors (AMCs) that can be implemented using the mushroom-like Electromagnetic Band Gap (EBG) structure in **Figure 1a**. The design of PRGW has been well addressed in the literature, which starts by designing the EBG-cells to support the required bandgap over the operating

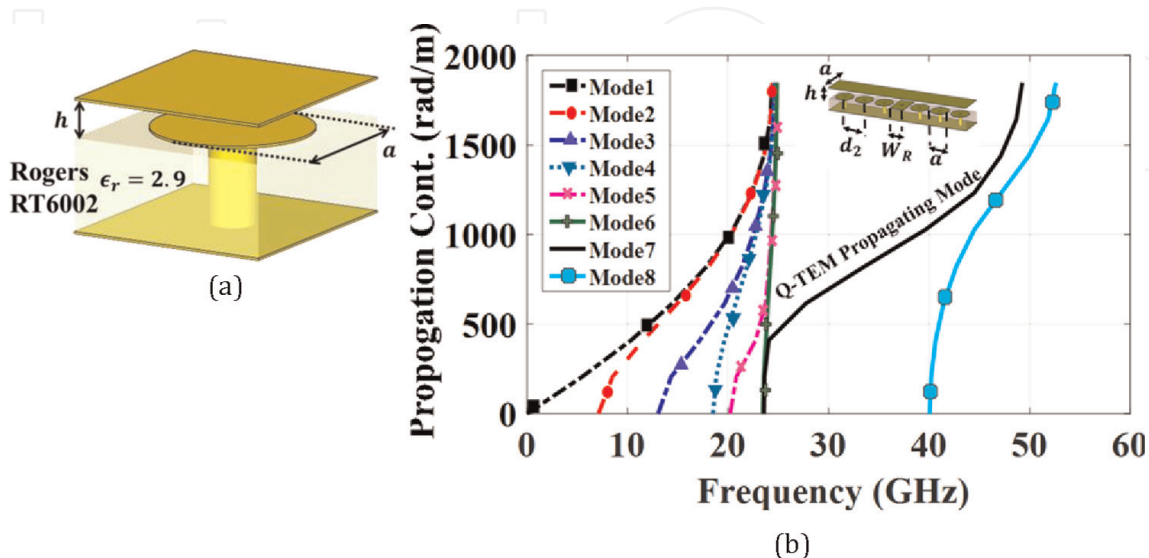


Figure 2. Design of electromagnetic band gap (EBG) structure. (a) EBG unit cell. (b) PRGW line segment and simulated dispersion diagram showing the propagating Q-TEM mode.

Dimension	a	h	h_s	d_2	W_R
Value (mm)	1.32	0.289	0.3065	1.52	1.37

Table 1.
dimensions of unit cell in EBG structure designed for 26–40 GHz band.

bandwidth. **Figure 2a** shows the EBG unit cell used to design the PRGW feeding line, where the geometrical parameters are listed in **Table 1**. As shown in **Figure 2b**, modelling the cell on CST MWS simulation software proves to achieve a bandgap covering the entire mm-Wave Ka-band of 26–40 GHz [41].

This chapter is organized in four sections as follows: Section 2 introduces two main transitions, from microstrip line and from coaxial line to PRGW that allow the integration with other technologies. Section 3 focuses on the design of PRGW hybrid couplers, crossovers, and phase shifters, which are the main building blocks of the beam switching networks. Section 4 discusses several designs of antenna elements and arrays with various polarizations and excitation techniques. The integration of the previous components to form a beam scanning antenna system will be discussed in Section 5, while the last section concludes the introduced material.

2. Transitions

To ensure the full integrability of the PRGW technology with other TEM guiding structures such as microstrip and coaxial lines, several types of PRGW transitions have been proposed in the literature correspondingly [42, 43]. The microstrip line to PRGW is considered the most simple and straightforward transition that can be used to excite the PRGW with a deep matching level over a broad bandwidth. **Figure 3** shows the geometrical configuration of microstrip line to PRGW transition, where the PRGW is directly connected with the 50 Ω microstrip line through a taper transformer with length L_t and width W_t [44, 45]. These two parameters are then optimized to adjust the matching level over the operating bandwidth, where the optimum dimensions are listed in **Table 2**. The operation of the transition is assessed using a PRGW bend junction as shown in **Figure 3a**. Comparison between the simulated and measured S-parameter results are shown in **Figure 3c**, where a matching level below -15 dB over the operating frequency bandwidth is achieved. It can be noticed that the measured insertion loss of this type of transition reaches -1 dB, where a large part of these losses results from the microstrip line radiation losses. This results in an inaccurate assessment of the PRGW devices through using this type of transition [44, 45].

Therefore, another type of transition, from coaxial to PRGW, is proposed to reduce the radiation losses, with the configuration illustrated in **Figure 4**. Such transition is useful in many circumstances where the PRGW device is the first component in the system taking the feed from the output coaxial terminal of the source. Like the previous design, mushroom shape periodic patch cells are used for emulating the artificial magnetic conductor. Two substrate materials are used in this multilayer configuration with an empty region in one substrate to provide the air gap [46]. Additionally, a group of metal vias is drilled around the transition to the ground plane to enhance the device performance [46]. The design dimensions are optimized to cover the whole band of 24–42 GHz and are listed in **Table 3**, while the simulation and measurement results in **Figure 4c** assess that operation.

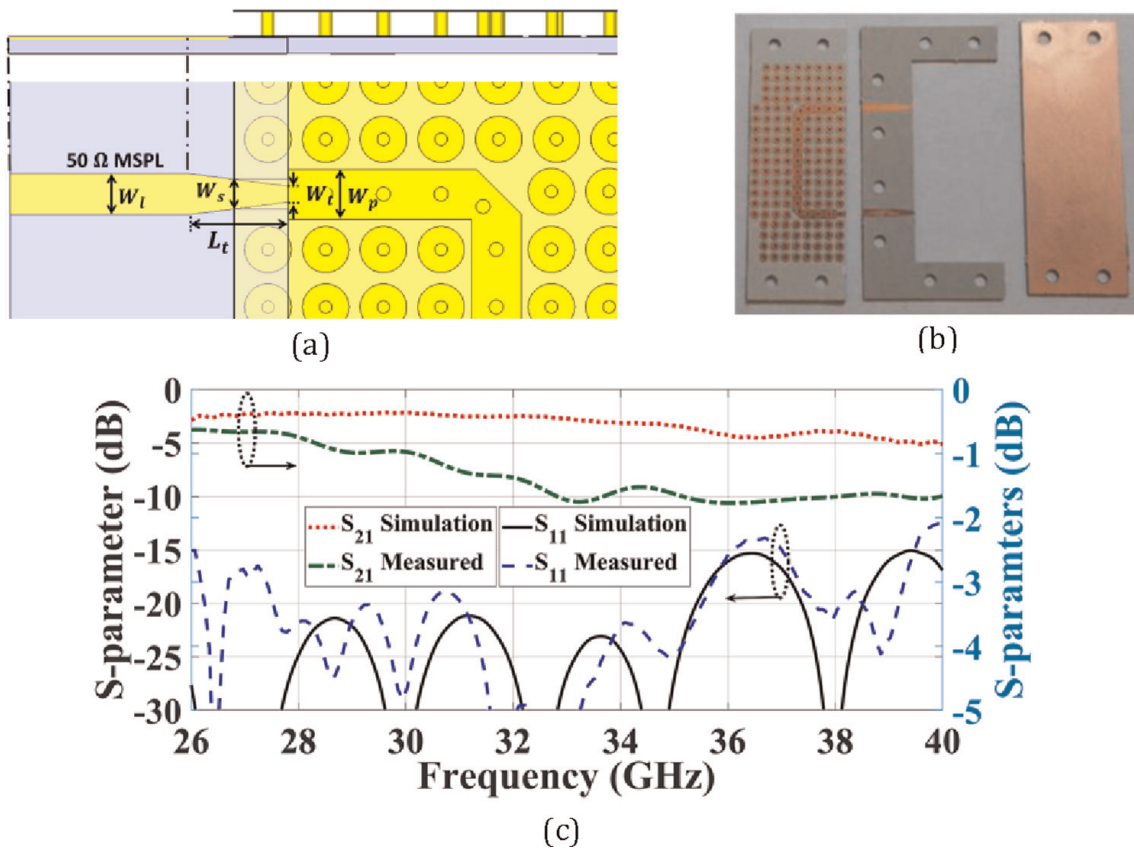


Figure 3. Microstrip to printed ridge gap waveguide transition. (a) Front and side views of the model. (b) Fabricated transition. (c) simulated and measured S-parameter responses.

Dimension	L_t	W_t	W_s	W_l	W_p
Value (mm)	3.045	0.5	0.946	1.265	1.55

Table 2. Dimensions of the microstrip\PRGW transition illustrated in Figure 3.

3. Feeding structures

3.1 Hybrid couplers

Hybrid couplers are the main building blocks of the beam switching network, which is used to divide the power equally with 90° phase shift and high isolation between the ports [47]. The design and analysis of several PRGW hybrid couplers configurations have been proposed in the literature, where two featured designs will be discussed in this section as are mainly deployed in beam switching antenna systems [45, 48–50].

The first design is shown in Figure 5, where four identical PRGW lines are connected through a rectangular coupling section with dimensions $(L \times W)$. These dimensions mainly control the coupling in the desired operating bandwidth, where the initial dimensions are calculated through applying the even/odd mode analysis [49]. Since the impedance of the four PRGW ports is different from the impedance of the coupling section, a taper matching transformer is introduced to achieve a deep matching level over the operating frequency band, where the final dimensions of the

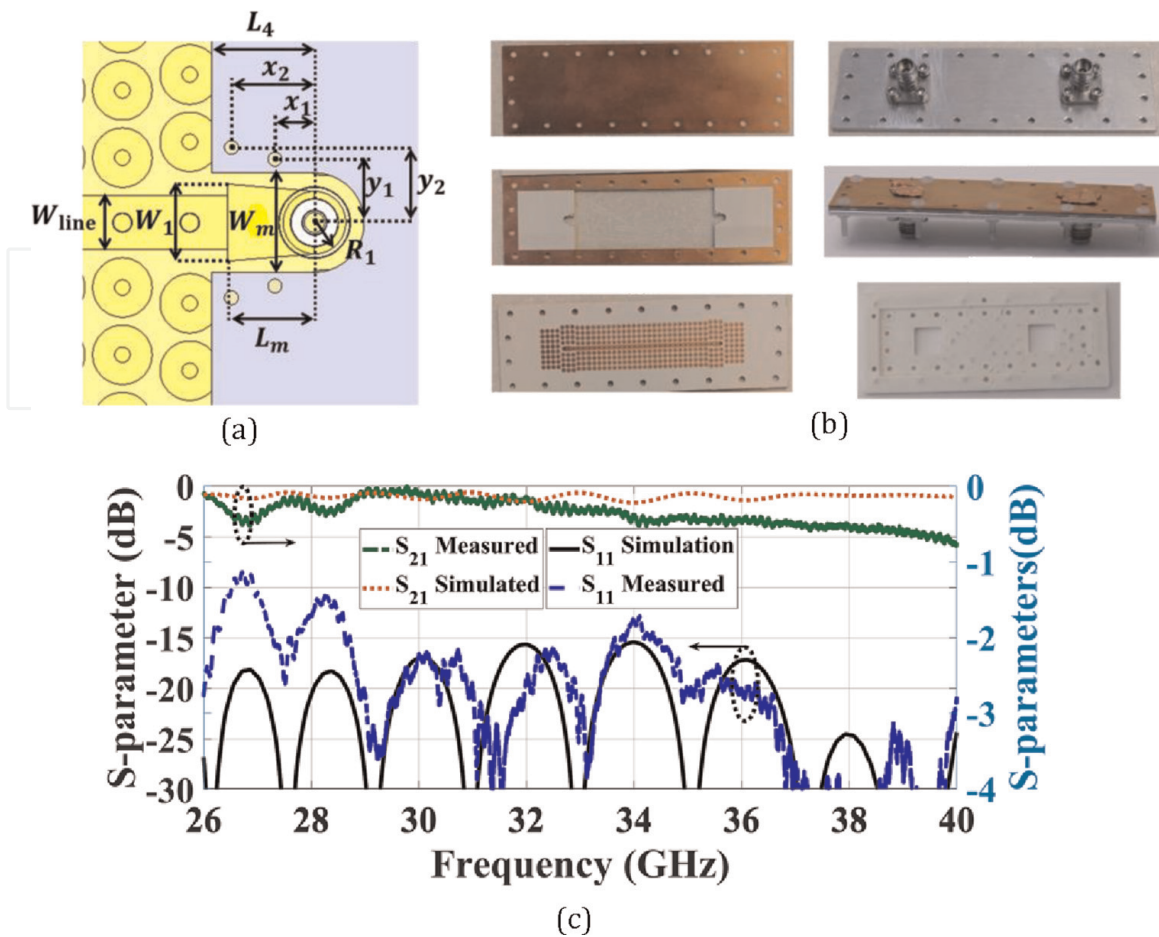


Figure 4. The design of coaxial to PRGW transition. (a) transition section with detailed dimensions. (b) fabricated layers. (c) simulated and measured results of the scattering parameters.

Dimension	R_1	L_m	W_1	W_{line}	a	d_{via}	d_{cap}	h_{pin}
Value (mm)	0.79	2.2	1.95	1.38	1.7	0.39	1.5	2.8
Dimension	L_4	W_2	d_{via1}	L_{line}	x_1	y_1	x_2	y_2
Value (mm)	2.6	2.508	0.35	52.2	1	1.6	1.1	1.9

Table 3. Dimensions of the coaxial to PRGW transition in Figure 4.

coupler are listed also in **Table 4**. The performance of the coupler is evaluated through simulation, where -15 dB matching level and isolation over a relative bandwidth of 26.5% at 30GHz are achieved as shown in **Figure 5b**. In addition, $90^\circ \pm 5^\circ$ phase shift is achieved between the output ports over the whole operating bandwidth [49]. However, one major drawback of this coupler is the amplitude imbalance ($3.5 \text{ dB} \pm 1.5$) is large, where high performance beam switching systems require both precise amplitude and phase balance over the operating frequency band.

Therefore, an alternative model targeting the same frequency band is presented in **Figure 6a**, where a circular coupling section is used rather than the rectangular junction in the former design [51]. The circular junction consists of two rings with different radii representing the widths of the equivalent branched line directional coupler. A bowtie shape slot is introduced in the center of the rings with specific

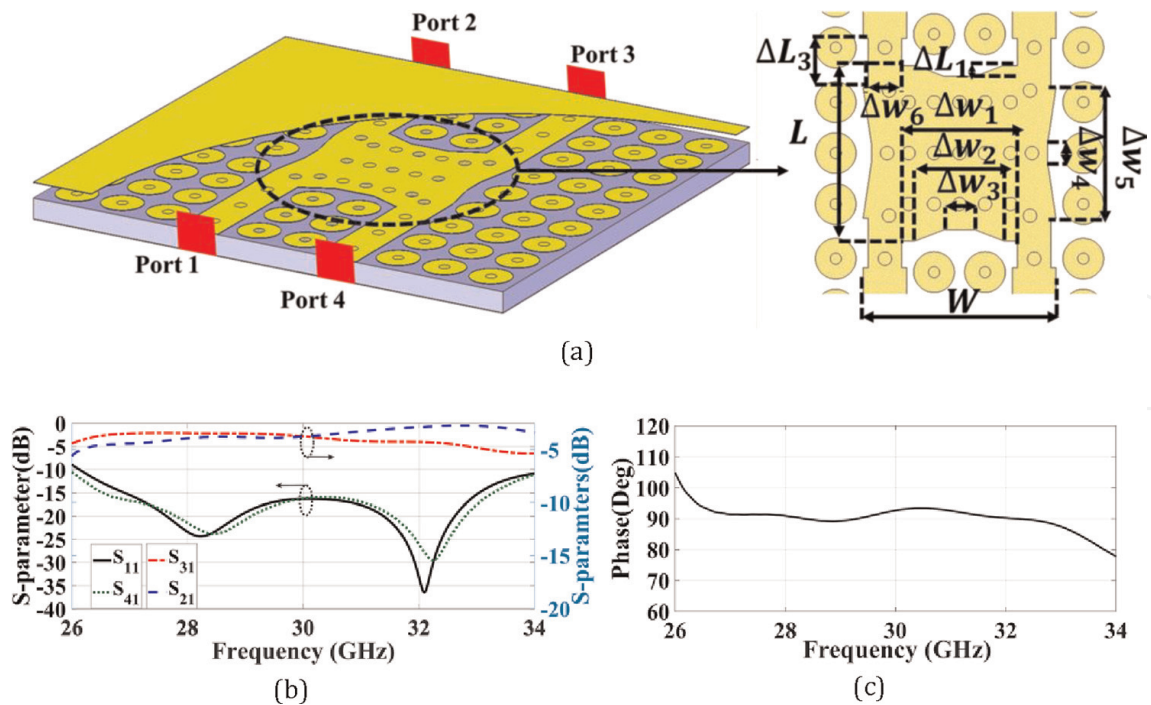


Figure 5. Quadrature 3 dB hybrid coupler: (a) design details and dimensions. (b) S -parameters simulation results. (c) phase difference of output ports.

Parameter	W	L	ΔL_1	ΔL_3	Δw_1	Δw_2	Δw_3	Δw_4	Δw_5	Δw_6
Value (mm)	6.7	6.1	0.32	2.1	4.1	3	1.1	0.7	4.5	0.9

Table 4. Dimensions of the coupling section illustrated in Figure 5a.

orientation to adjust the coupler performance [51]. Furthermore, a step matching section is added to each transmission line to adapt the impedances over the operating band. The design depends on the suitable adjustment of each ring width, the bowtie slot, and the dimensions of the matching section. These parameters are given in Table 5, while the simulation results are illustrated in Figure 6b and c proving efficient operation over the frequency range of 26.4–33.75 GHz. As an assessment of the advantage of PRGW technology over other new technologies, Table 6 summarizes a comparison among the performance of the rectangular hybrid coupler in Figure 5 and other designs in the literature.

3.2 Crossover

Beam switching networks impose the usage of crossover connections when two PRGW lines cross each other at a point while at the same time must be totally isolated [55, 56]. Two main techniques can be used to implement crossovers, and two featured designs will be presented in this section [51, 57].

The first design is based on the traditional technique of cascading 3 dB directional couplers to implement the crossover. However, three quarter wavelength sections are used to widen the bandwidth more than that of the traditional designs which use two sections only [51]. Using three cascaded sections introduces more design variables and more degrees of freedom to optimize the performance. The analysis of the structure is

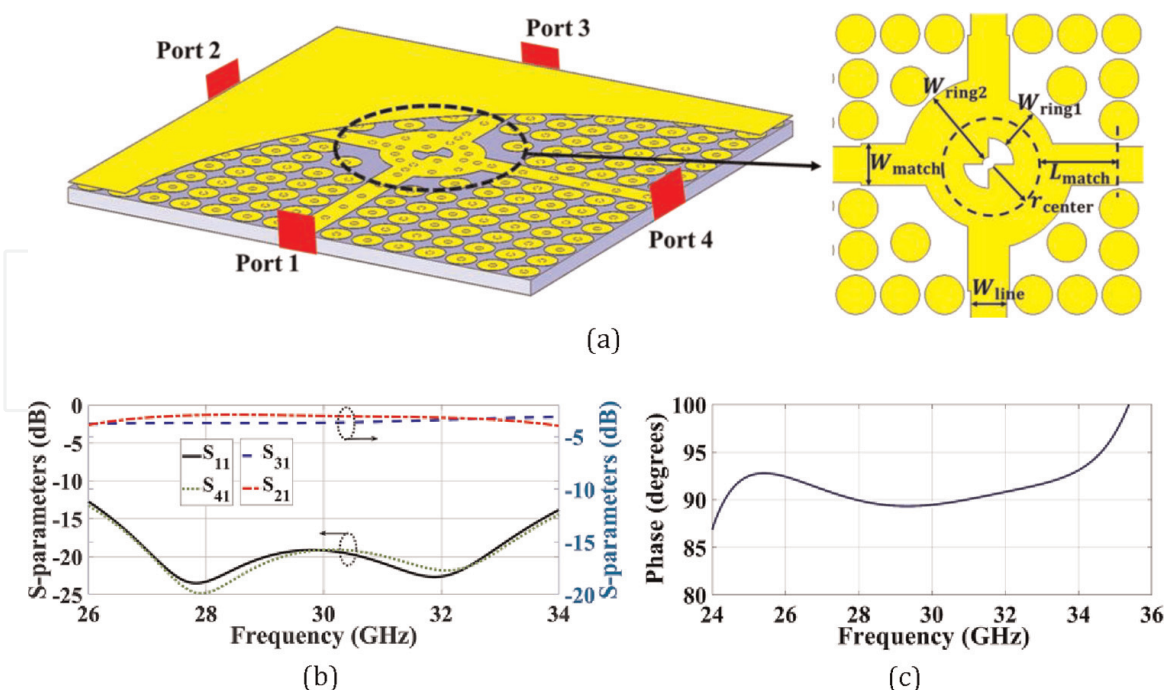


Figure 6. Design and performance of the ring coupler. (a) design details and dimensions (b) full S-parameters for a single port. (c) phase difference between output ports.

Parameter	W_{line}	W_{match}	L_{match}	r_{center}	W_{ring1}	W_{ring2}
Value (mm)	1.38	1.582	3.14	1.753	1.595	3.05

Table 5. Dimensions of the design in Figure 6a.

done by even\odd mode analysis, and the design parameters are optimized for minimum isolation and reflection [58]. The design is shown in **Figure 7a** and **b**, while the parameters are given in **Table 7**. As seen by the results in **Figure 7c**, the device achieves a relative bandwidth of 23% at 30 GHz with more than 15 dB isolation.

A disadvantage of the traditional technique of using cascaded couplers is the large size of the crossover. Aiming to avoid that common shortage, another model is presented in **Figure 8a**. This design is based on achieving 0 dB coupling in a directional coupler by designing even and odd impedances with 5% difference between each other over the frequency band of interest [57]. The design has the structure of four PRGW lines connected through a rectangular coupling section in the middle. By suitable choice of the dimensions of the coupling section, full isolation can be ensured between a single port and two of the four ports, yielding 0 dB coupling with the remaining port [57]. Multiple steps are added in the coupling section as tuning parameters to enhance the operating bandwidth [57]. The final dimensions of these steps and the coupling section are given in **Table 8**, for which the device produces the S-parameters illustrated by **Figure 8c** and obtained through CST simulation. These results indicate acceptable operation over the frequency range of 28.5–32.5 GHz in terms of isolation and coupling. The device achieves relative bandwidth of about 13.3%, which is typically higher than usual single layer crossover designs of the same size. Moreover, comparison with designs from other technologies is listed in **Table 9**, featuring the advantages of both the compact size and high relative bandwidth obtained by PRGW technology.

Reference	Technology	Impedance bandwidth	Amplitude balance (dB)	Phase balance	Size ($\lambda_0 \times \lambda_0$)
[52]	Rectangular waveguide	6.5% at 14 GHz	3.1 ± 0.2 BW = 6.5%	$90^\circ \pm 0.3^\circ$ BW = 6.5%	1.6×1.7
[53]	Substrate integrated waveguide (SIW)	18% at 24 GHz	4.7 ± 0.5 BW = 10%	$92^\circ \pm 2^\circ$ BW = 18%	1.4×1.5
[54]	Half mode SIW	11% at 27.5 GHz	4.8 ± 0.25 BW = 7%	$180^\circ \pm 10^\circ$ BW = 11%	Not included
	Proposed PRGW	26% at 30 GHz	3.7 ± 0.75 BW = 13%	$90^\circ \pm 5^\circ$ BW = 23%	1.3×1.1

Table 6.
 Comparison of PRGW hybrid coupler design with other technologies.

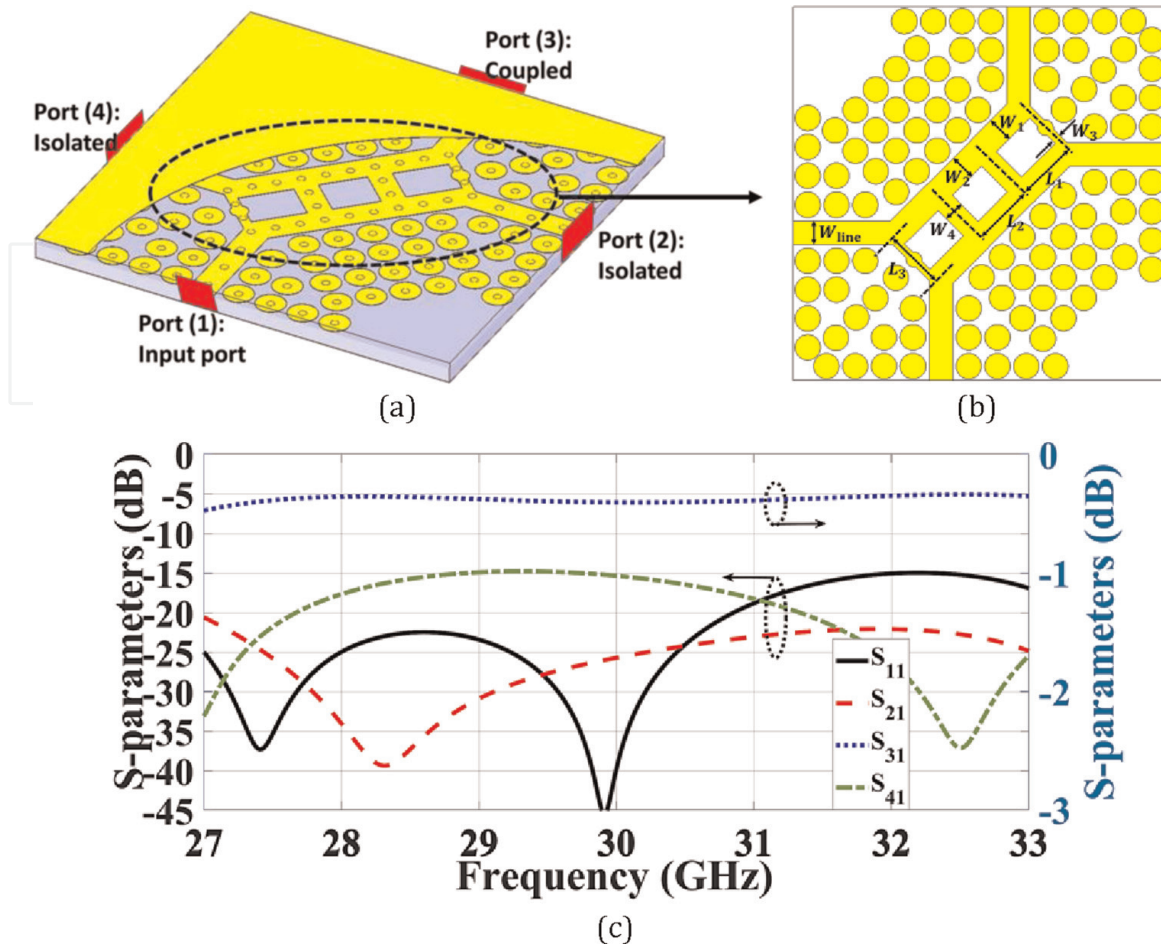


Figure 7. Crossover design by cascaded couplers. (a) 3D view of the PRGW crossover. (b) details and dimensions of the cascaded couplers. (c) simulated S-parameter response of the crossover along isolation and coupling directions.

Parameter	W_{line}	W_1	W_2	W_3	W_4	L_1	L_2	L_3
Value (mm)	1.38	1.56	1.49	0.52	1.23	3.65	3.65	3.65

Table 7. Parameters of the crossover illustrated by Figure 7b.

3.3 Phase shifters

Phase shifters are essential components in Butler matrices, implemented to provide the required phase difference between the antennas in the beam scanning arrays. For efficient beam control, the introduced phase shift must be stable over the operating bandwidth with low insertion loss, where several techniques have been investigated in the literature to achieve that property [47, 61]. One technique is based on using four port directional couplers with the isolated and through ports connected to each other. This produces the well-known Schiffman phase shifter for which the differential phase shift can be adjusted through careful selection of impedances of the coupled lines [62].

Figure 9a illustrates a Schiffman phase shifter based on PRGW technology, designed to achieve a 45° differential phase shift around 30 GHz [62]. Widths of the input and output lines, as well as those of the coupled section were all designed using

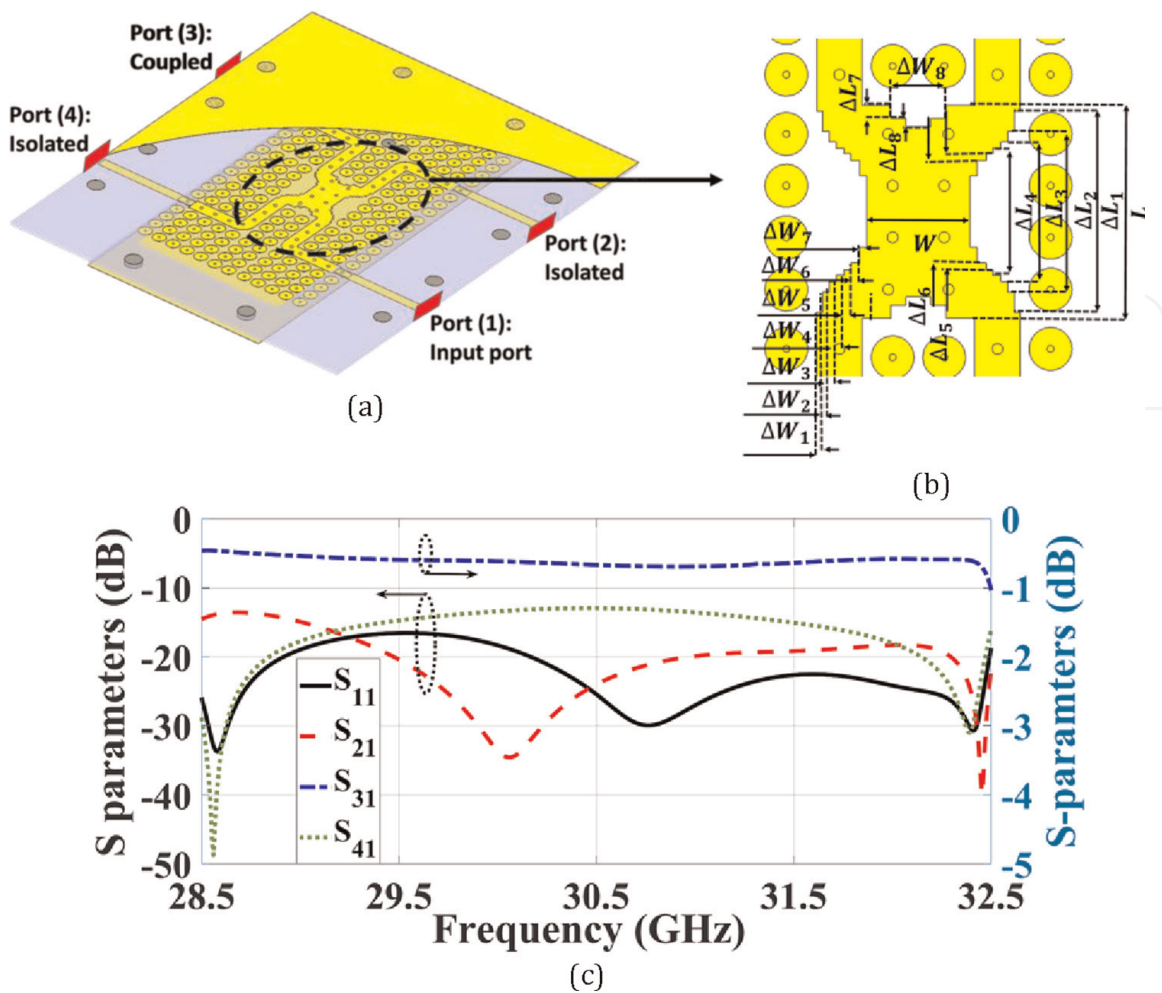


Figure 8. Design of 0 dB coupler using rectangular coupling section to provide a crossover around 30 GHz. (a) 3D view of the crossover. (b) details of the coupling section. (c) simulated S-parameters assessing the isolation and coupling around 30 GHz.

Coupling Section	Step		1	2	3	4	5	6	7	8
W	8	ΔL_i	7.5	6	5.2	4.7	4.3	3.8	0.5	0.3
L	10	ΔW_i	0.22	0.24	0.26	0.31	0.25	0.33	0.26	0.92

Table 8. Dimensions (in mm) of the coupling section and the matching steps in the crossover of Figure 8b.

Reference	Technology	Center frequency	Bandwidth	Insertion Loss (dB)	Size (λ^2)
[59]	SIW	20 GHz	10.5%	—	2
[60]	Slot SIW	30 GHz	16.7%	0.9	3.1
	Proposed PRGW	30 GHz	13.3%	0.5	2.25

Table 9. Comparison of a proposed PRGW crossover with other technologies.

even\odd mode analysis of directional couplers [58]. The length of the coupled section was optimized for increased operating bandwidth. Final dimensions are given in Table 10, while the simulated S-parameters response is given in Figure 9b. The

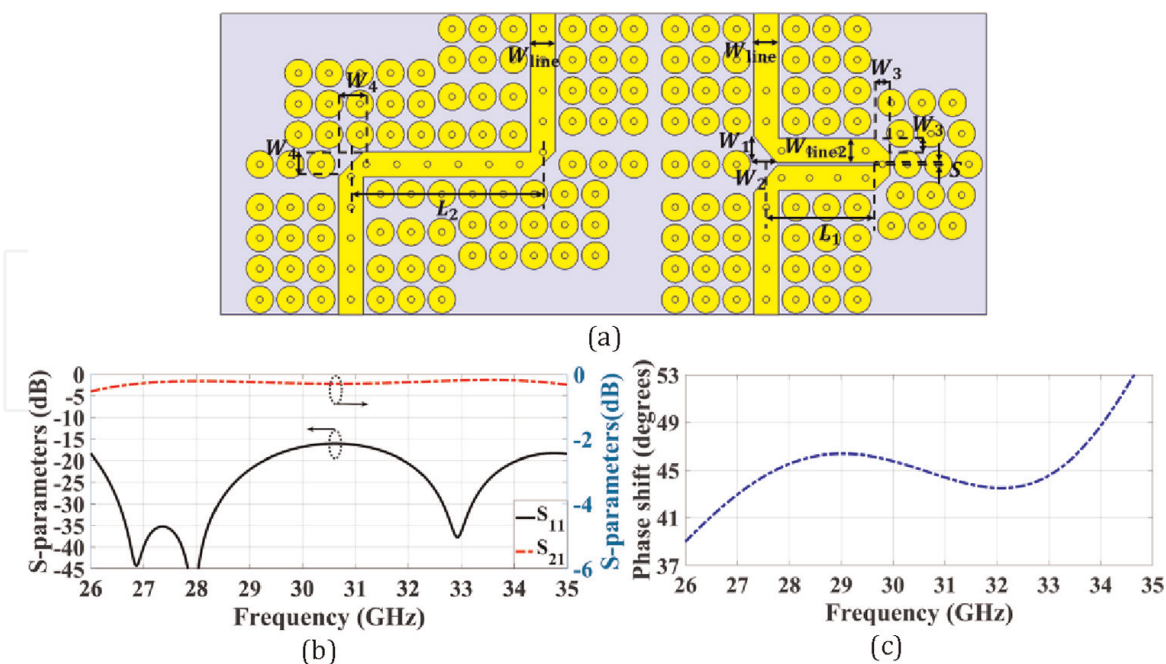


Figure 9. Design and performance of the Schiffman 45° phase shifter. (a) detailed design dimensions. (b) simulated S-parameters magnitude. (c) phase difference between the input and output ports.

Parameter	W_{line}	W_{line2}	W_1	W_2	W_3	W_4	L_1	L_2	S
Value (mm)	1.38	1.35	1.49	1.28	0.88	1.4	5.99	10.64	0.15

Table 10. Dimensions of the Schiffman phase shifter illustrated in **Figure 9a**.

device achieves 21.7% relative bandwidth at 30 GHz with 45° phase shift $\pm 2.5^\circ$ differential phase error and less than 0.4 dB insertion loss [62].

3.4 Differential feeding power dividers

One of the main targets of mm-Wave beam switching arrays is to overcome the multipath fading in wireless communication channels by using space or polarization diversity techniques [9, 10]. These diversity techniques require the array to have highly stable radiation characteristic and low cross polarization level [61]. Such demands impose the usage of differential feeding for the array elements, which can be provided through out of phase power dividers. In this section, two designs for differential feeding power dividers are introduced.

The first design is shown in **Figure 10a**, where the power divider is implemented using two layers of PRGW structure coupled by I-shaped slot [63]. The first layer has the input feeding line connected to a matching stub optimized to achieve a deep matching level over a wide bandwidth, while the upper layer contains the two output PRGW lines, where the coupling through the I-shaped slot achieves the 180° phase difference [63]. The design dimensions are listed in **Table 11**, and the simulated S-parameters response shown in **Figure 10b** reveals a 20% relative bandwidth with more than 15 dB return loss and less than 0.3 dB insertion loss over the whole operating bandwidth. The phase difference between the output ports is stable around 180° ensuring differential output.

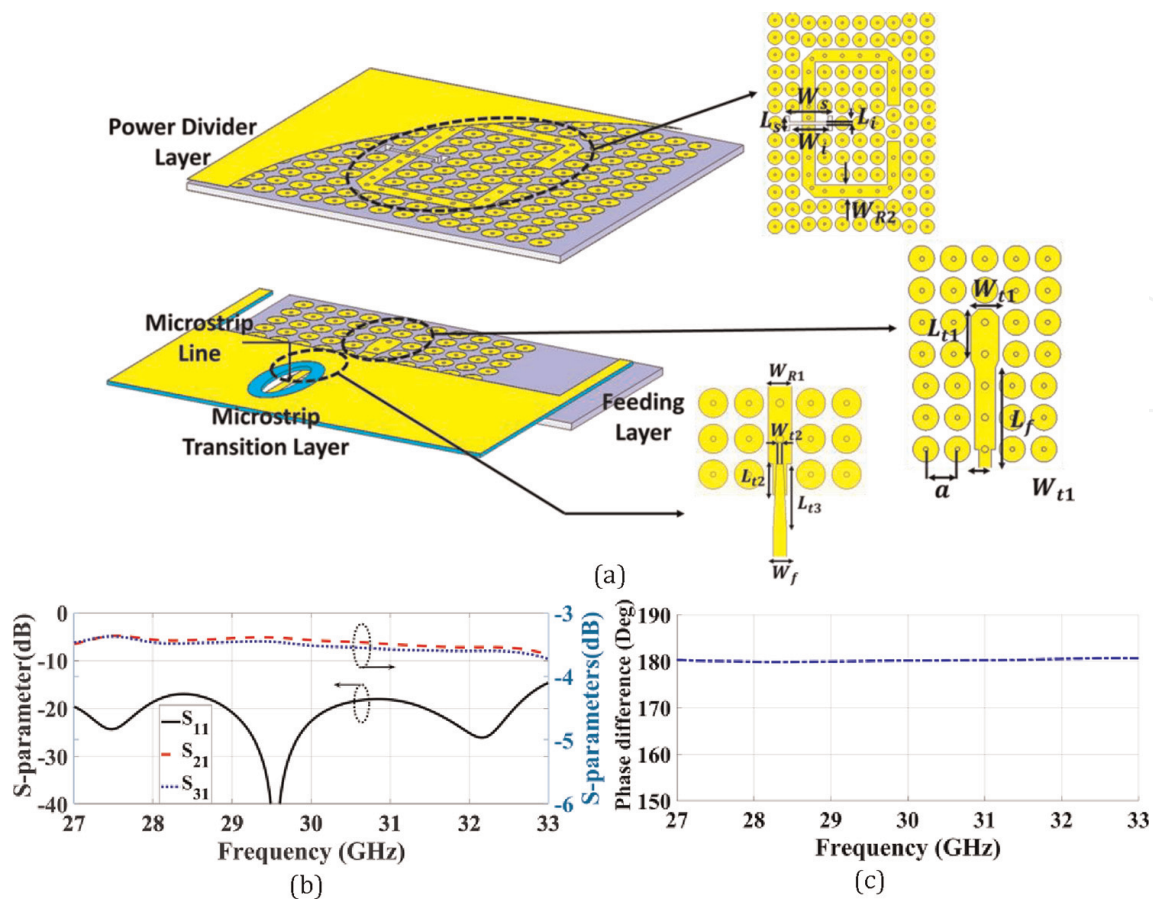


Figure 10. Power divider design (a) detailed design dimensions for the feeding and divider layers. (b) Simulated S-parameters. (c) Phase difference between output ports.

Parameter	a	L_{t1}	W_{t1}	L_f	W_f	L_s	W_s
Value (mm)	1.8	2.85	1.6	5.5	0.65	1.9	5
Parameter	L_i	W_i	W_{R1}	W_{R2}	h_1	h_2	h_3
Value (mm)	0.34	4	1.37	1.37	0.5	0.5	0.127

Table 11. Dimensions of the power divider in Figure 10a.

An alternative design is shown in Figure 11a where a hybrid ring or rat-race directional coupler is used to satisfy the power divider function with 180° in the output phase shift [64]. One advantage of rat-race couplers is that they can be used to produce in-phase or out-phase feeding according to the choice of the input port. The illustrated design has an introduced open circuited stub at the middle of the $3\lambda/4$ part of the ring which controls the signal splitting ratio between the output ports. Furthermore, at each port of the coupler, a quarter wavelength transformer is added to enhance the relative bandwidth [64]. The design dimensions of the ring, the stub and the quarter transformers are given in Table 12. With these dimensions, the device achieves 27.69% bandwidth at 30 GHz with more than 15 dB isolation as shown by the S-parameters in Figure 11b. A brief comparison is listed in Table 13 among the former rat race coupler and other designs based on SIW technology, revealing the promising performance of the PRGW design.

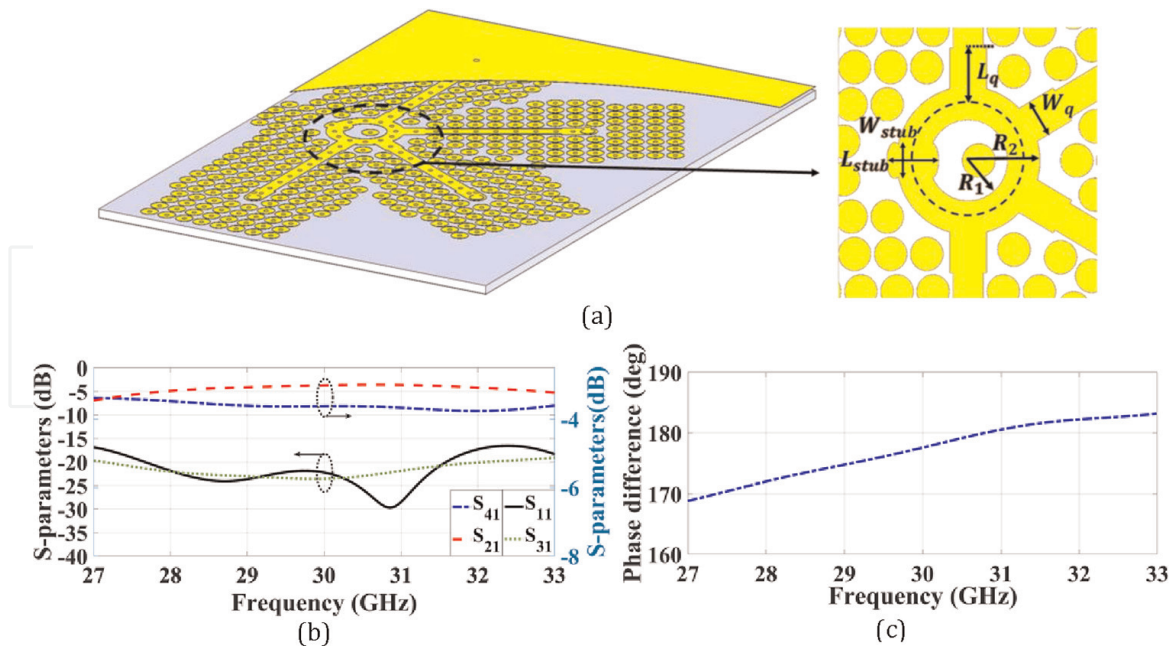


Figure 11. Rat-race coupler design. (a) design with details and dimensions. (b) simulated S-parameters. (c) Phase difference between output ports.

Parameter	L_q	W_q	L_{stub}	W_{stub}	R_1	R_2
Value (mm)	2.5	1.7	2.4	0.8	1.85	3.35

Table 12. Values of the rat-race coupler dimensions illustrated by **Figure 11a**.

Reference	Technology	Center frequency	Bandwidth	Return loss (dB)	Insertion loss (dB)	Amplitude balance (dB)
[65]	SIW	13 GHz	30%	18	20	3.35 ± 1.35
[66]	Half mode SIW	10.15 GHz	24.6%	12	15	3.8 ± 0.5
[67]	T-type folded SIW(TFSIW)	25.7 GHz	12.7%	20	20	4.3 ± 0.6
[68]	RSIW	8 GHz	12.5%	12	20	3.79 ± 0.5
	Proposed PRGW	30 GHz	27.9%	15	16.5	3.39 ± 0.5

Table 13. Comparison with other technologies design for power dividers.

4. Antenna structures

The use of antenna arrays in communication handsets is feasible in mm-Wave communications due to the inherently small size of the antennas. However, applying diversity techniques in these systems require specific properties of the antennas, like stable and controllable radiation patterns, and the ability to produce a desired polarization with low cross polarization level. In this section, we present different antenna designs covering the

possible polarizations, namely linear, circular, and dual polarizations as candidates for mm-Wave applications. The presented designs show promising performance in terms of beam stability, wide bandwidth, and low cross polarization level.

4.1 Linearly polarized antenna

As shown in **Figure 12**, a linearly polarized planar aperture antenna is presented, based on a similar design [69]. The antenna aperture has a cross-shaped patch in the middle, all in one top layer, fed by capacitive coupling from a differential feeding line in a bottom layer [58, 69]. The benefit of using planar radiating aperture is the ability to produce highly directive beam without need for increased dimensions. The feeding line is tapered and loaded with stubs to achieve acceptable matching level. The dimensions of the radiating element and the feeding structure are tuned to achieve optimum bandwidth, in terms of return loss and beam stability over the band [58]. The final dimensions are given in **Table 14**, while simulated and measured reflection coefficient and realized gain are plotted in **Figure 12c**. To obtain the measured results, the fabricated antenna was fed by the rat-race directional coupler, described in the previous section, to provide the differential feeding signal [64]. The results, as shown by **Figure 12c**, reveal a wide bandwidth

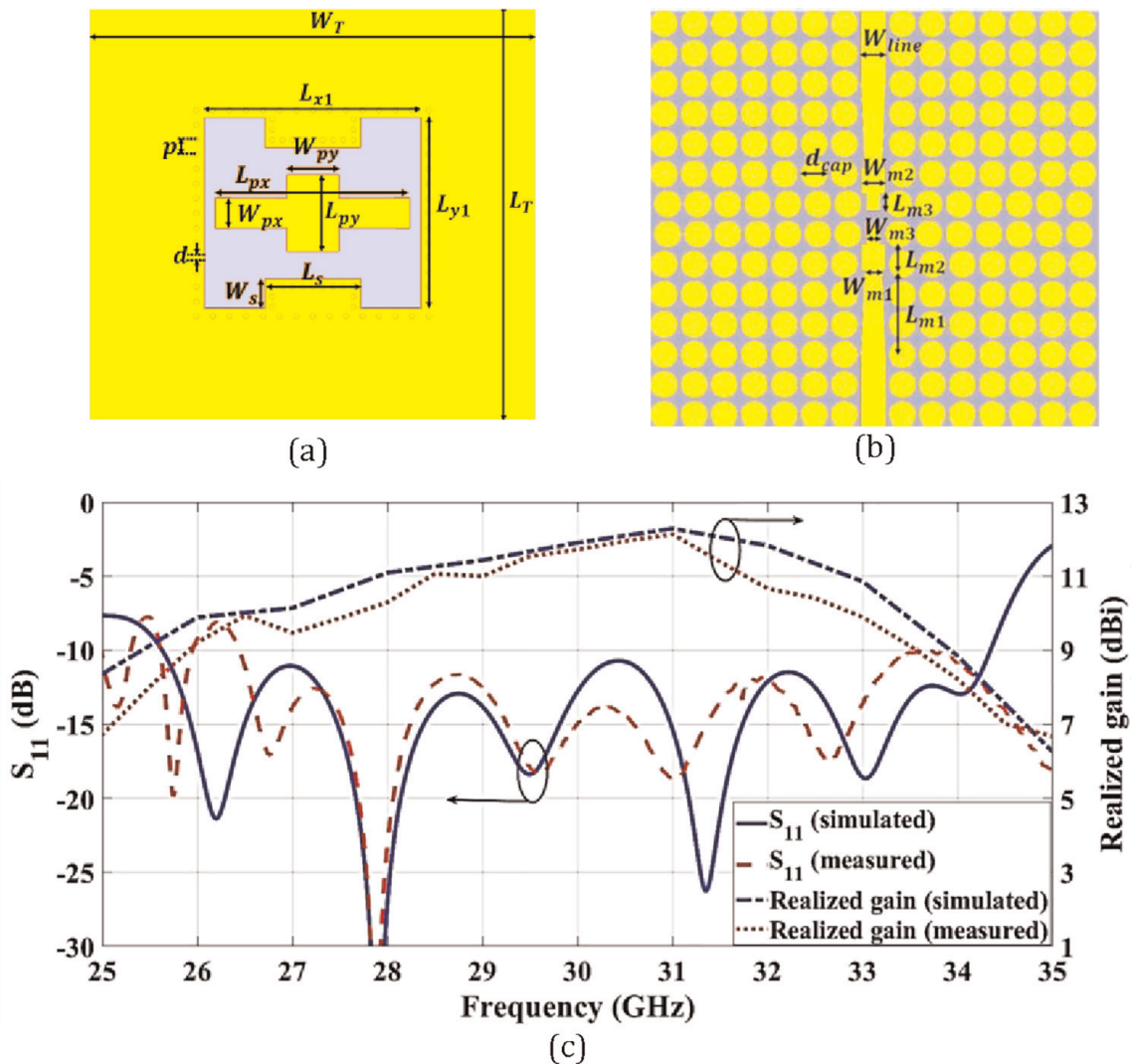


Figure 12. Linearly polarized planar aperture antenna. (a) Top view. (b) bottom view. (c) simulated and measured S-parameter and realized gain.

Dimension	L_T	W_T	L_{x1}	L_{y1}	L_{px}	L_{py}	W_{px}	W_{py}	p	W_{line}
Value (mm)	23.8	25.5	12.45	10.94	11.09	4.36	1.7	2.97	0.84	1.38
Dimension	d	L_s	W_s	L_{m1}	L_{m2}	L_{m3}	W_{m1}	W_{m2}	W_{m3}	d_{cap}
Value (mm)	0.3	5.47	1.68	4.83	1.49	0.94	0.95	1.33	1.38	1.5

Table 14. Dimensions of the planar aperture antenna and its differential feeding layer shown in **Figure 12a** and **b**.

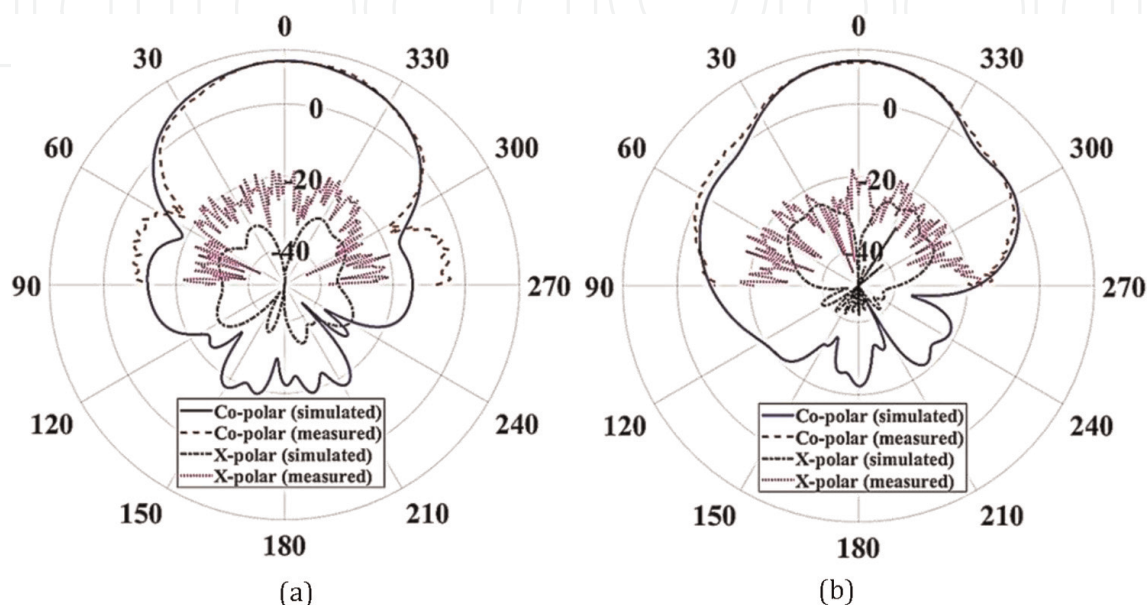


Figure 13. Radiation properties of the linearly polarized planar aperture antenna. (a) simulated and measured co- and x- polarization patterns in E-plane at 30 GHz. (b) simulated and measured co- and x- polarization patterns in H-plane at 30 GHz.

over 25.6–34.3 GHz band with more than 10 dB return loss and with 12.28 dB_i maximum gain. Moreover, the 3 dB gain bandwidth covers the range from 25.6 GHz up to 33.7 GHz, indicating a stable beam of the antenna. Beam stability is further revealed by measuring the radiation pattern at multiple frequencies over the band [58]. The simulated and measured patterns at the center frequency of 30 GHz are shown in **Figure 13a** and **b**. These patterns illustrate a very low cross polarization level in both E- and H- planes.

4.2 Circularly polarized antenna

Alternatively, the antenna design illustrated in **Figure 14** provides circular polarization (CP) at the same frequency band around 30 GHz. Unlike typical CP antenna designs, which depend on feeding the radiating element by two equal amplitude and quadrature phase signals, this design uses differential feeding to a planar aperture loaded with a polarizer [63]. The polarizer consists of an annular ring with two opposite cuts adjacent to the feeding position. These cuts perturb the excitation and cause the formulation of two orthogonal modes. The circular polarization is then adjusted through the circular patch added at the center to tune the amplitude and the phase relation of these orthogonal modes [63]. This tuning is performed by adjusting the patch size, and the orientation of the two introduced non-radiating edge slots. The antenna is designed on

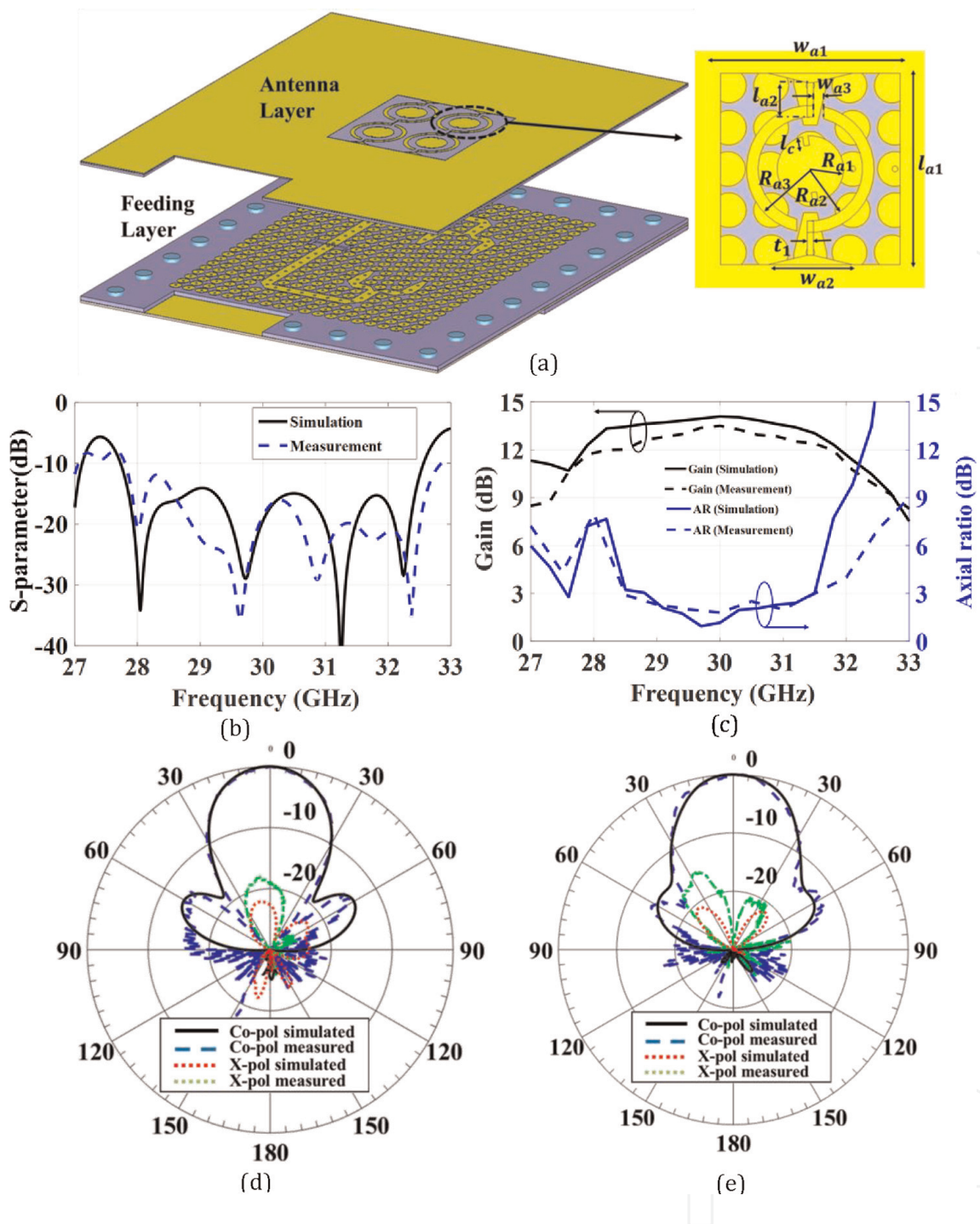


Figure 14. Design and performance of the CP antenna: (a) design details. (b) simulated and measured $|S_{11}|_{dB}$. (c) simulated and measured gain and axial ratio over the band. (d) simulated co- and x- polarization patterns (RH and LH CP's) in E-plane. (e) simulated co- and x- polarization patterns (RH and LH CP's) in H-plane.

the Rogers RT5880 substrate with 0.127 mm thickness and 2.2 relative permittivity [63]. All the design dimensions are given in **Table 15**, for the planar aperture, the polarizer, and the patch in the center. Since this antenna is mainly aimed for use in communication arrays, the performance is investigated for an array of 4 elements shown by the 3D view of the design layers in **Figure 14a**. The simulated and measured reflection coefficients of that array are given in **Figure 14b** and indicate below -10 dB reflection over the 28–32.5 GHz frequency range, which is equivalent to 15% relative bandwidth at 30 GHz. Simulated and measured axial ratio illustrated in **Figure 14c** is showing 3 dB axial ratio

Dimension	w_{a1}	l_{a1}	w_{a2}	l_{a2}	w_{a3}	t_1	l_c	R_{a1}	R_{a2}	R_{a3}
Value (mm)	8.2	8.6	3.7	1.47	0.5	0.26	0.4	1.45	2.36	2.85

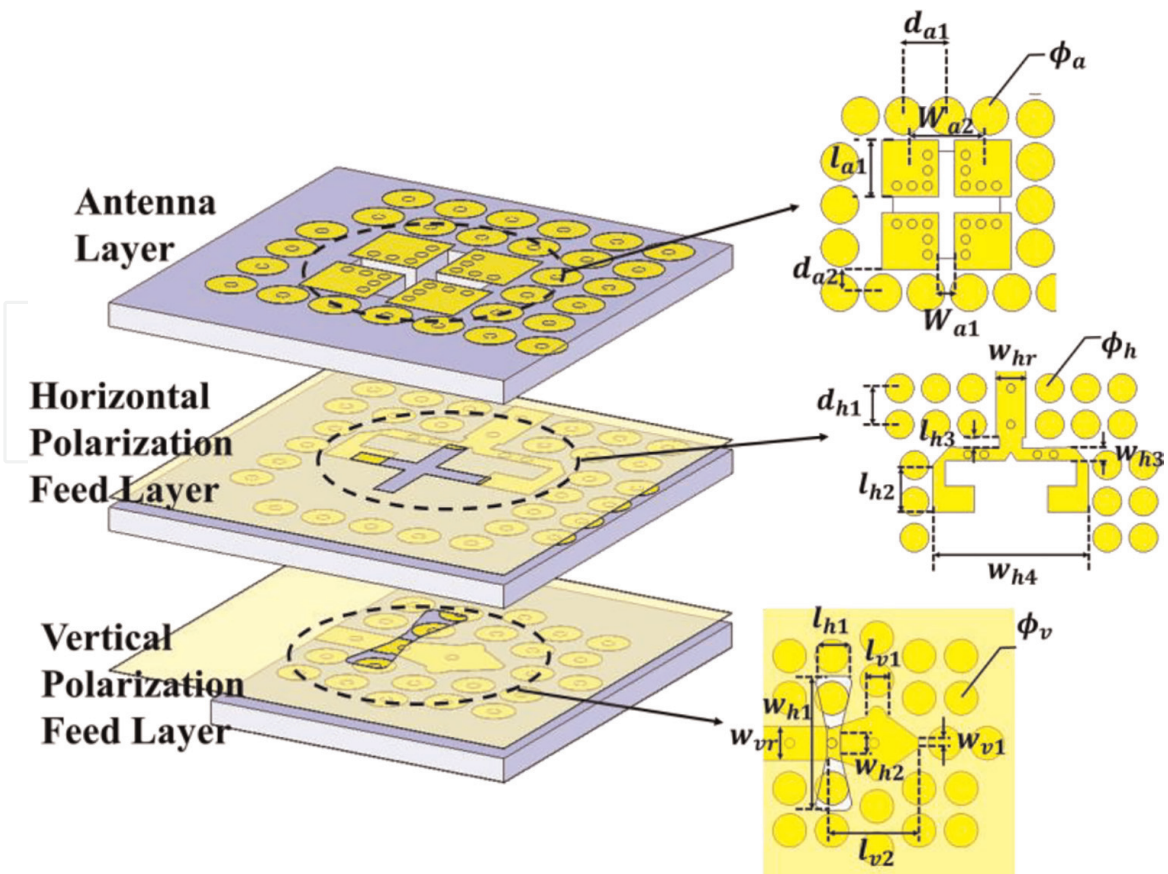
Table 15.

Dimensions of the circularly polarized antenna illustrated by **Figure 14a**.

over 28.5–31.5 GHz range, a slightly smaller relative bandwidth of 10%. However, these achievements are greater than the usually narrow bandwidths for CP antennas reported at 30 GHz. Regarding the cross polarization level and the beam angle, simulated and measured radiation patterns at 30 GHz are plotted in **Figure 14d** and **e**, showing less than -20 dB cross polarization levels at the direction of maximum radiation [63].

4.3 Dual polarized antenna

Finally, a dual polarized antenna is presented in **Figure 15**, where horizontal and vertical polarizations can be excited from two different isolated ports [70]. The two isolated ports are in different layers as shown in **Figure 15**. The antenna structure is implemented on the top layer and consists of two orthogonal magneto electric (ME) dipoles in the vertical and in the horizontal directions. Therefore, vertical and horizontal linear polarizations are obtained upon exciting the antenna. Each ME dipole is formed by means of two square patches, connected to the ground by five conducting plates at the patch corner [70]. This configuration, when excited properly, formulates an electric dipole from the plates, and a dual magnetic dipole from the vias. The structure in **Figure 15** has then two vertical and horizontal dipoles of each type [70].


Figure 15.

ME dipole antenna design and detailed dimensions of each layer.

Parameter	w_{a1}	w_{a2}	w_{h1}	w_{h2}	w_{h3}	w_{h4}	w_{v1}	w_{vr}	w_{hr}	ϕ_a	ϕ_h
Value (mm)	0.5	4.1	5.6	1	0.75	7.3	0.4	1.37	1.37	1.6	1.3
Parameter	l_{h1}	l_{h2}	l_{h3}	l_{a1}	l_{v1}	l_{v2}	d_{a1}	d_{a2}	d_{h1}	ϕ_v	
Value (mm)	0.6	1.6	1.5	2.5	0.9	3.2	1.8	1	1.7	1.3	

Table 16.
 Dimensions of the magneto-electric dipole antenna and its feeding structure illustrated in Figure 15.

Among the benefits of using ME dipole antennas are the directive pattern obtained identically in the E- and H-planes, and the stable beam of the antenna as to be illustrated in the subsequent results. **Table 16** summarizes the design dimensions of the ME dipole antenna and its feeding structure.

Figure 16a illustrates the simulated and measured S-parameters of this dual polarization ME dipole antenna. With respect to the self-matching of each port, the antenna achieves more than 10 dB return loss over 26.5–33.5 frequency range, which is approximately equivalent to 23% relative bandwidth at 30 GHz [70]. The isolation between the two ports exceeds 20 dB over the band. The simulated and measured gain values for each port are given in **Figure 16b**, indicating around 10 dB_i gain for each polarization [70]. The stability of the antenna beam is tested by measuring and simulating the radiation pattern at different frequency values, of which the results at 30 GHz are shown in **Figure 16c** and **d**. These drawn patterns are in E- and H- planes for the two co-polarizations along with their corresponding x-polarization level. The antenna achieves less than –20 dB x-polarization in each case, proving a great performance for polarization diversity applications [70].

5. Beamforming techniques

Beamforming is performed by means of a beam switching network (BSN) or a butler matrix which controls the signal feeding to/from the antennas in the array. The essential components constituting BSNs are the phase shifters, hybrid couplers, power dividers and crossovers discussed in the former sections. Upon introducing these components, we present two designs of butler matrices in this section and the deployment of these matrices to design beam scanning antenna arrays.

Figure 17a shows a 4×4 butler matrix realized by four directional couplers to distribute the signals, with the desired phase relations, between the four feeding ports and the four array elements [71]. Various designs of hybrid couplers are presented in Section 3.1, which cover the whole desired band of 27–33 GHz. This 4×4 butler matrix achieves two-dimensional beam scanning in the horizontal plane. The obtainable beam directions are $\theta_0 = 45^\circ$ and $\phi_0 = -45^\circ, 45^\circ, 135^\circ$ and -135° for excitations from Ports 1, 2, 3 and 4 respectively. The performance of this matrix is first evaluated in terms of ports' matching and isolation. Simulated and measured scattering parameters of Port 1 are shown in **Figure 17b** where more than 10 dB return loss and isolation is obtained over the band. These levels are then expected for all other ports due to the design symmetry. To test the scanning abilities, the matrix is used to feed an array of four ME-dipole antennas and the radiation pattern is simulated and measured [71]. The array shows a measured realized gain of 9.7 ± 0.4 dB_i where the reduction from the simulated results is mainly caused by feeding network losses. The simulated and measured radiation patterns in $\phi = -45^\circ$ and $\phi = 135^\circ$ planes are given for Port 1 and Port 3

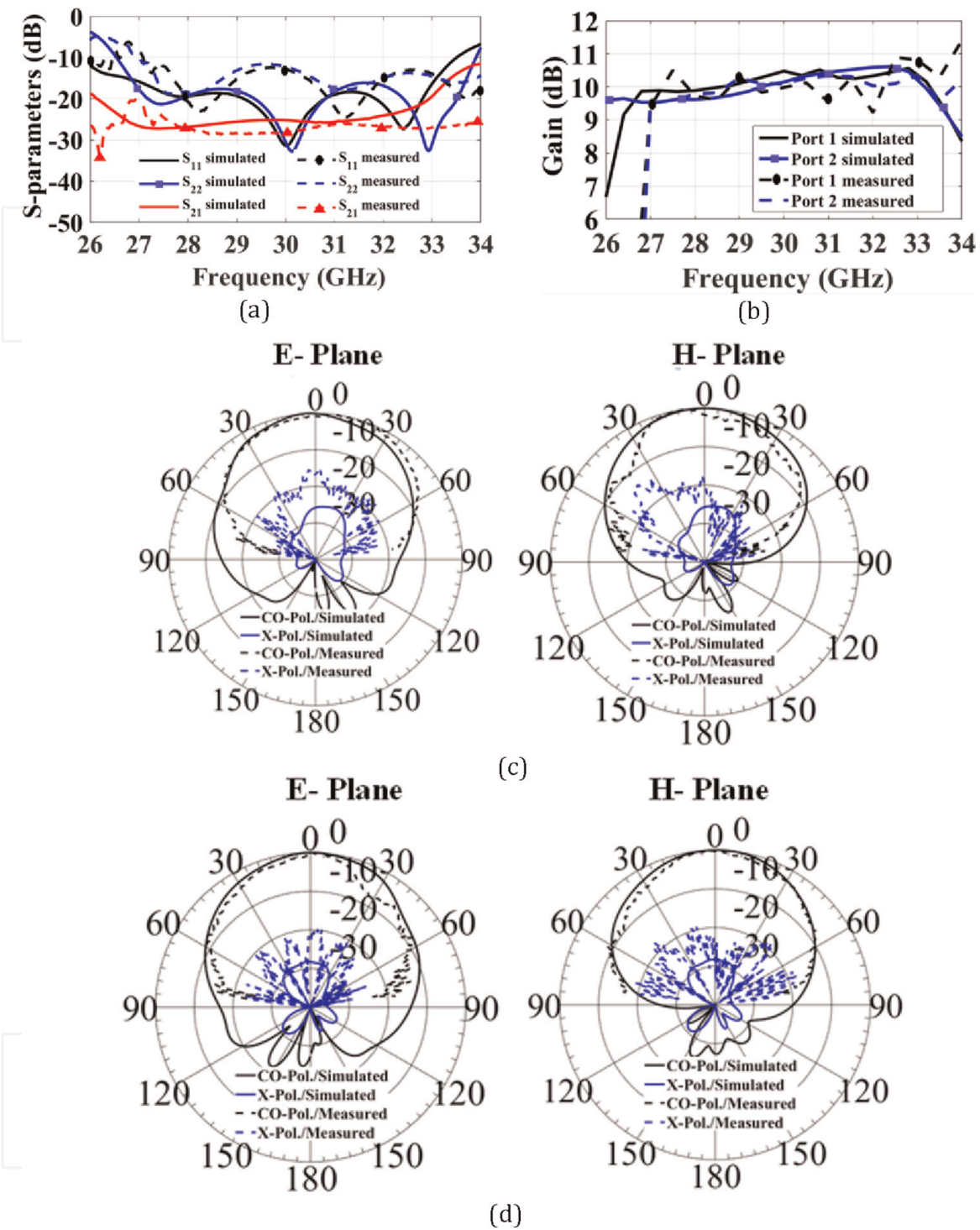


Figure 16. Magneto-electric dipole antenna performance. (a) simulated and measured S -parameters. (b) simulated and measured gain over the band. (c) simulated and measured radiation patterns at 30 GHz for horizontal polarization in E- and H-planes. (d) simulated and measured radiation patterns at 30 GHz for vertical polarization in E- and H-planes respectively.

excitations. The beam is nearly identical, emphasizing efficient scanning, with low cross-polarization level of less than -20 dB at the main direction [71].

An alternative 4×4 butler matrix is shown in **Figure 18a**, where the ring power divider, cascaded crossover and the Schiffman phase shifter described in the previous sections are all integrated in one network [51]. The four input ports to the matrix are all coaxial ports where coaxial to PRGW transition are used. The matrix is feeding four

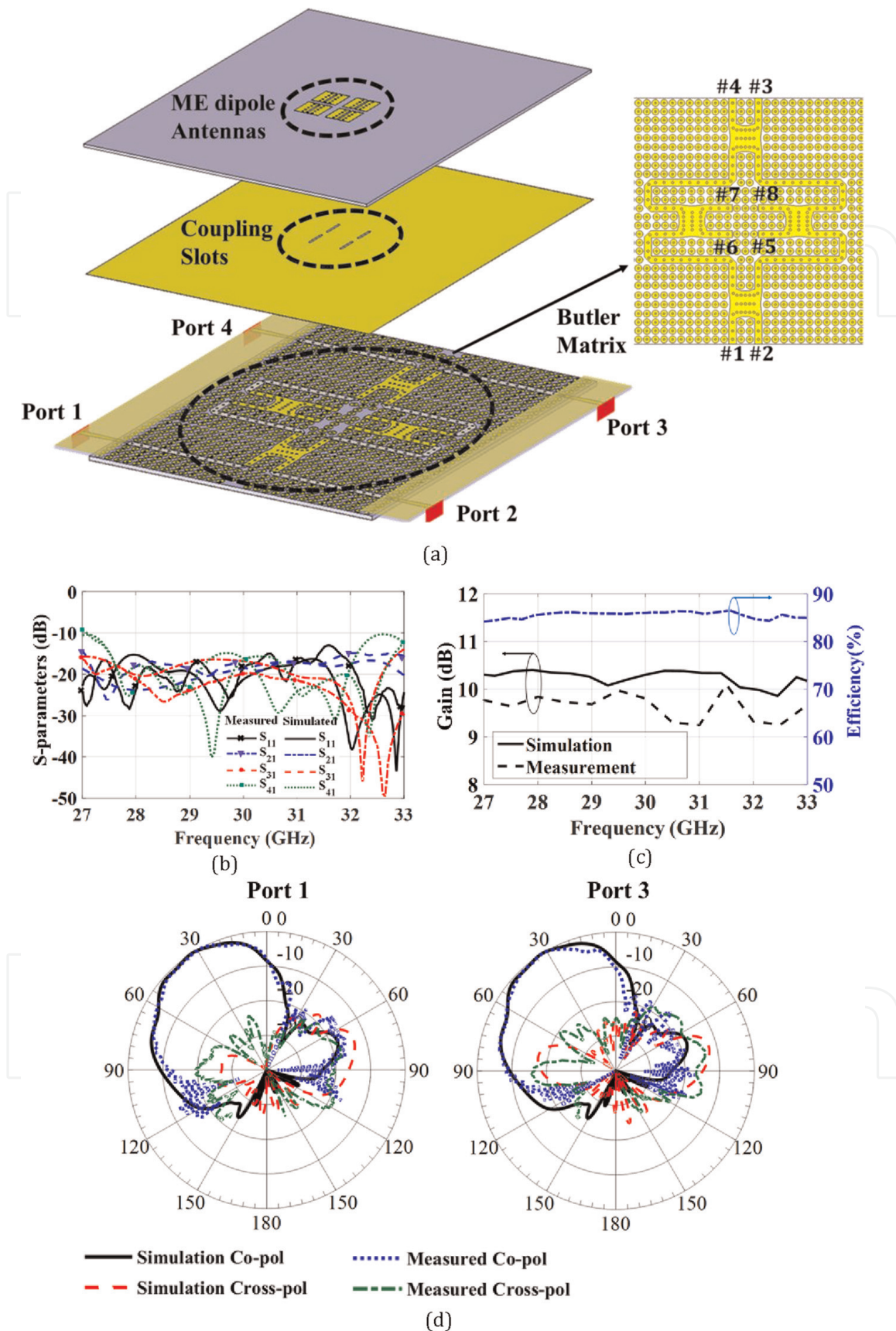


Figure 17. 4×4 butler matrix, realized by four directional couplers, and achieves 2D beam scanning. (a) detailed 3D view of the matrix and the fed antennas. (b) simulated and measured reflection coefficient and isolation of the first port. (c) simulated and measured gain and efficiency over the band. (d) simulated and measured radiation pattern at $\phi = -45^\circ$ with Port 1 excited (left) and at $\phi = 135^\circ$ with Port 3 excited (right).

wideband semi-log periodic dipole antennas to test the array performance [72]. Since the radiating elements are all printed antennas with microstrip feeding input, MSPL to PRGW transition is used at each matrix output. Two secondary antennas are added to enhance the symmetry of the radiation pattern.

The array performance is illustrated by **Figure 18b–d**. The simulated and measured scattering parameters indicate isolation and return loss levels of more than 10 dB over the frequency range of 26–34 GHz. The array achieves radiation efficiency of 78% with gain value ranging from 10 dB_i to 11.35 dB_i over the whole frequency band (for excitation from port 1). The obtainable angles of the beam are -13° , -36° , 36° , and 13° for excitation from ports 1, 2, 3, and 4 respectively [51]. The simulated and measured gain patterns in **Figure 18d** are obtained at 30 GHz and emphasize the scanning ability of the array.

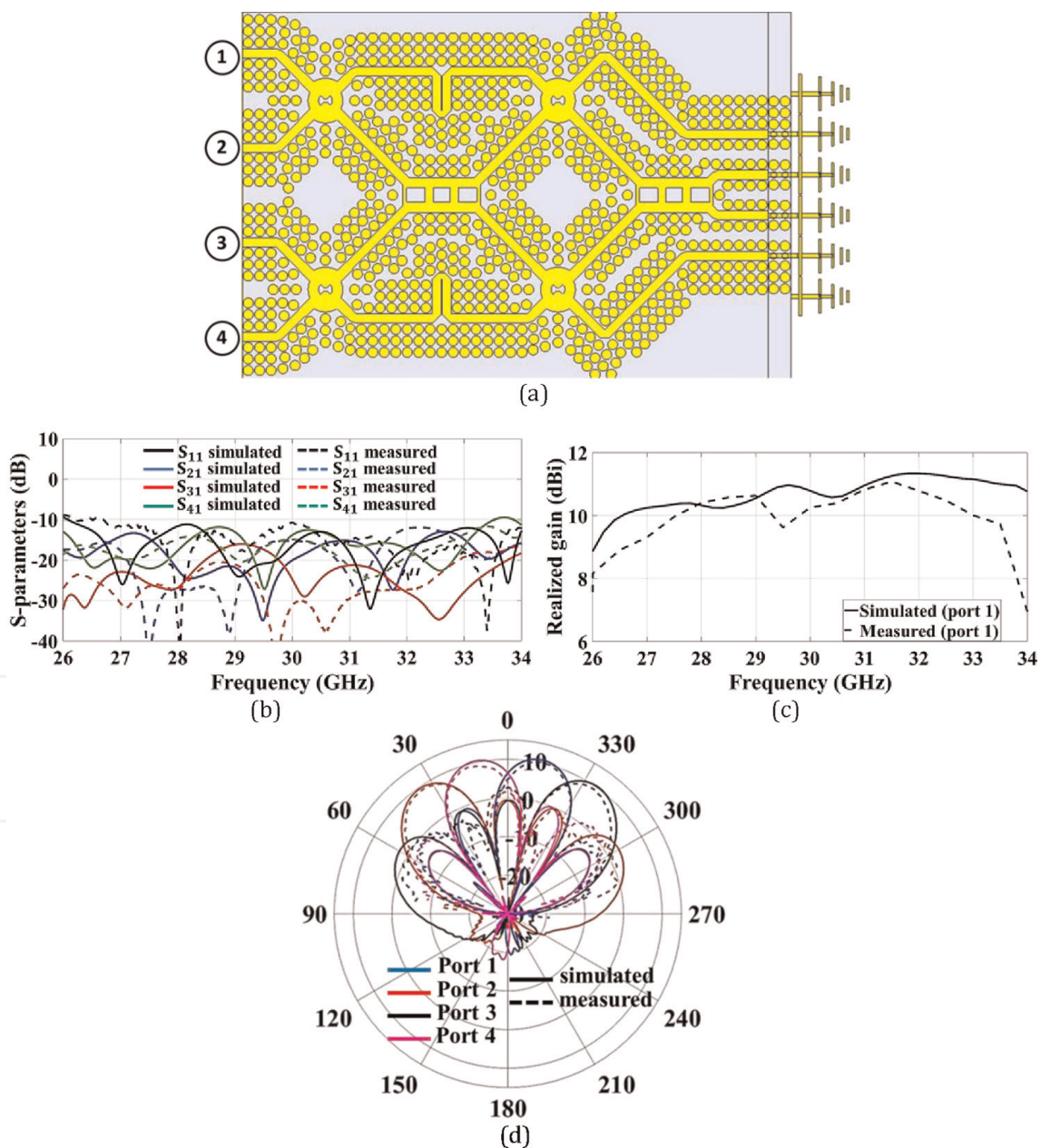


Figure 18. Design and performance of the second 4×4 butler matrix for beam switching network. (a) design details. (b) simulated and measured reflection and isolation for Port 1. (c) simulated and measured realized gain for Port 1. (d) simulated and measured radiation pattern for the excitation from the four ports.

6. Conclusions

Printed ridge gap waveguide is an emerging technology with powerful capabilities that allow designing efficient beam switching networks for mm-Wave communications. In this chapter, various PRGW components designed for beam switching arrays at 30 GHz are presented. First, we present transitions to\from other guiding standards like coaxial and MSPL structures. These transitions provide efficient integration with these guiding standards. Then, hybrid couplers with rectangular and circular coupling sections are introduced. Crossover designs are also provided with various design techniques; either using multistage directional couplers or using compact single stage stepped design. A Schiffman phase shifter with 45° phase shift is also presented. Differential power dividers are introduced, one relying on slot coupling to two identical lines and the other depending on rat race design. The chapter also presents different designs of antennas covering all possible polarizations. It is then revealed how the usage of PRGW technology can provide efficient excitation of antennas with different polarizations and design profiles. Full beam switching networks are presented in the last section, where two different 4×4 butler matrices are introduced with their usage in achieving the beam scanning function of the array. Assessment of these various devices reveals the promising performance of the new PRGW structure over other competing technology candidates. The new PRGW technology can give better performance in terms of device size, bandwidth and fabrication costs.

Author details

Mohammad Ali AbdElraheem¹, Mohamed Mamdouh M. Ali^{2*}, Islam Afifi³
and Abdel R. Sebak¹


1 Concordia University, Montreal, Canada

2 Assiut University, Assiut, Egypt

3 Cairo University, Cairo, Egypt

*Address all correspondence to: mohamed.ali@ieee.org

IntechOpen

© 2022 The Author(s). Licensee IntechOpen. This chapter is distributed under the terms of the Creative Commons Attribution License (<http://creativecommons.org/licenses/by/3.0>), which permits unrestricted use, distribution, and reproduction in any medium, provided the original work is properly cited. 

References

- [1] ITU-T Recommendations and other publications [Internet]. ITU. 2022. Available from: <https://www.itu.int:443/en/ITU-T/publications/Pages/default.aspx>
- [2] IEEE Standard for Air Interface for Broadband Wireless Access Systems. IEEE Std 80216-2012 Revis IEEE Std 80216-2009. 2012;1–2542
- [3] Tehrani RH, Vahid S, Triantafyllopoulou D, Lee H, Moessner K. Licensed spectrum sharing schemes for mobile operators: A survey and outlook. *IEEE Communications Surveys and Tutorials*. 2016;**18**(4): 2591-2623
- [4] Jameel F, Hamid Z, Jabeen F, Zeadally S, Javed MA. A survey of device-to-device communications: Research issues and challenges. *IEEE Communications Surveys and Tutorials*. 2018;**20**(3):2133-2168
- [5] Chen R, Long WX, Mao G, Li C. Development trends of mobile communication systems for railways. *IEEE Communications Surveys and Tutorials*. 2018;**20**(4):3131-3141
- [6] Baltaci A, Dinc E, Ozger M, Alabbasi A, Cavdar C, Schupke D. A survey of wireless networks for future aerial communications (FACOM). *IEEE Communications Surveys and Tutorials*. 2021;**23**(4):2833-2884
- [7] Xia N, Chen HH, Yang CS. Radio resource management in machine-to-machine communications—A survey. *IEEE Communications Surveys and Tutorials*. 2018;**20**(1):791-828
- [8] Agiwal M, Roy A, Saxena N. Next generation 5G wireless networks: A comprehensive survey. *IEEE Communications Surveys and Tutorials*. 2016;**18**(3):1617-1655
- [9] Xiao M, Mumtaz S, Huang Y, Dai L, Li Y, Matthaiou M, et al. Millimeter wave communications for future mobile networks. *IEEE Journal on Selected Areas in Communications*. 2017 Sep;**35**(9):1909-1935
- [10] Rappaport TS, Sun S, Mayzus R, Zhao H, Azar Y, Wang K, et al. Millimeter wave mobile communications for 5g cellular: It will work! *IEEE Access*. 2013;**1**:335-349
- [11] Rappaport TS, Murdock JN, Gutierrez F. State of the Art in 60-GHz integrated circuits and systems for wireless communications. *Proceedings of the IEEE*. 2011 Aug;**99**(8):1390-1436
- [12] Chettri L, Bera R. A comprehensive survey on internet of things (IoT) toward 5G wireless systems. *IEEE Internet of Things Journal*. 2020;**7**(1): 16-32
- [13] Meinel HH. Commercial applications of millimeterwaves: History, present status, and future trends. *IEEE Transactions on Microwave Theory and Techniques*. 1995;**43**(7):1639-1653
- [14] Pereira de Figueiredo FA. An overview of massive MIMO for 5G and 6G. *IEEE Latin America Transactions*. 2022;**20**(6):931-940
- [15] Wang X, Kong L, Kong F, Qiu F, Xia M, Arnon S, et al. Millimeter wave communication: A comprehensive survey. *IEEE Communications Surveys and Tutorials*. 2018;**20**(3):1616-1653
- [16] Rangan S, Rappaport TS, Erkip E. Millimeter-wave cellular wireless networks: Potentials and challenges.

Proceedings of the IEEE. 2014;**102**(3):
366-385

[17] Shafi M, Molisch AF, Smith PJ, Hausteint T, Zhu P, De Silva P, et al. 5G: A tutorial overview of standards, trials, challenges, deployment, and practice. *IEEE Journal on Selected Areas in Communications*. 2017;**35**(6):1201-1221

[18] Rappaport TS, Gutierrez F, Ben-Dor E, Murdock JN, Qiao Y, Tamir JI. Broadband millimeter-wave propagation measurements and models using adaptive-beam antennas for outdoor urban cellular communications. *IEEE Transactions on Antennas and Propagation*. 2013;**61**(4):1850-1859

[19] Gupta A, Jha RK. A survey of 5G network: Architecture and emerging technologies. *IEEE Access*. 2015;**3**: 1206-1232

[20] Tataria H, Shafi M, Molisch AF, Dohler M, Sjöland H, Tufvesson F. 6G wireless systems: Vision, requirements, challenges, insights, and opportunities. *Proceedings of the IEEE*. 2021;**109**(7): 1166-1199

[21] Di Renzo M, Haas H, Ghayeb A, Sugiura S, Hanzo L. Spatial modulation for generalized mimo: Challenges, opportunities, and implementation. *Proceedings of the IEEE*. 2014;**102**(1): 56-103

[22] Islam SMR, Avazov N, Dobre OA, Kwak K, sup. Power-domain non-orthogonal multiple access (NOMA) in 5G systems: Potentials and challenges. *IEEE Communications Surveys and Tutorials*. 2017;**19**(2):721-742

[23] Natarajan A, Reynolds SK, Tsai MD, Nicolson ST, Zhan JHC, Kam DG, et al. A fully-integrated 16-element phased-array receiver in SiGe BiCMOS for 60-GHz communications. *IEEE Journal of*

Solid-State Circuits. 2011;**46**(5):
1059-1075

[24] Garg R, Natarajan AS. A 28-GHz low-power phased-array receiver front-end with 360° RTPS phase shift Range. *IEEE Transactions on Microwave Theory and Techniques*. 2017;**65**(11):4703-4714

[25] Moulder WF, Khalil W, Volakis JL. 60-GHz two-dimensionally scanning array employing wideband planar switched beam network. *IEEE Antennas and Wireless Propagation Letters*. 2010; **9**:818-821

[26] Ashraf N, Kishk AA, Sebak A. Broadband millimeter-wave beamforming components augmented with AMC packaging. *IEEE Microwave and Wireless Components Letters*. 2018; **28**(10):879-881

[27] Denlinger EJ. Losses of microstrip lines. *IEEE Transactions on Microwave Theory and Techniques*. 1980;**28**(6): 513-522

[28] Wu K, Bozzi M, Fonseca NJG. Substrate integrated transmission lines: Review and applications. *IEEE Journal of Microwaves*. 2021;**1**(1):345-363

[29] Lai Q, Fumeaux C, Hong W, Rü V. Characterization of the propagation properties of the half-mode substrate integrated waveguide. *IEEE Transactions on Microwave Theory and Techniques*. 2009;**57**(8):1996-2004

[30] Cassivi Y, Perregrini L, Arcioni P, Bressan M, Wu K, Conciauro G. Dispersion characteristics of substrate integrated rectangular waveguide. *IEEE Microwave and Wireless Components Letters*. 2002;**12**(9):333-335

[31] Xu F, Wu K. Guided-wave and leakage characteristics of substrate integrated waveguide. *IEEE*

Transactions on Microwave Theory and Techniques. 2005;53(1):66-73

[32] Kildal PS, Alfonso E, Valero-Nogueira A, Rajo-Iglesias E. Local metamaterial-based waveguides in gaps between parallel metal plates. IEEE Antennas and Wireless Propagation Letters. 2009;8:84-87

[33] Bayat-Makou N, Kishk AA. Realistic air-filled TEM printed parallel-plate waveguide based on ridge gap waveguide. IEEE Transactions on Microwave Theory and Techniques. 2018;66(5):2128-2140

[34] Sharifi Sorkherizi M, Kishk AA. Fully printed gap waveguide with facilitated design properties. IEEE Microwave and Wireless Components Letters. 2016;26(9):657-659

[35] Farahani M, Akbari M, Nedil M, Denidni TA, Sebak AR. A novel low-loss millimeter-Wave 3-dB 90° ridge-gap coupler using large aperture progressive phase compensation. IEEE Access. 2017; 5:9610-9618

[36] Sifat SM, Ali MMM, Shams SI, Sebak AR. High gain bow-tie slot antenna array loaded with grooves based on printed ridge gap waveguide technology. IEEE Access. 2019;7:36177-36185

[37] Dadgarpour A, Bayat-Makou N, Antoniadis MA, Kishk AA, Sebak A. A dual-polarized magnetolectric dipole array based on printed ridge gap waveguide with dual-polarized split-ring resonator lens. IEEE Transactions on Antennas and Propagation. 2020;68(5): 3578-3585

[38] Zhao Z, Denidni TA. Millimeter-wave printed-RGW hybrid coupler with symmetrical square feed. IEEE Microwave and Wireless Components Letters. 2020;30(2):156-159

[39] Kakhki MB, Dadgarpour A, Antoniadis MA, Sebak AR, Denidni TA. Magneto-electric dipole antennas loaded with meta-lens for 5G MIMO pattern diversity applications. IEEE Transactions on Antennas and Propagation. 2021;1-1

[40] Ali MMM, Al-Hasan M, Mabrouk IB, Denidni TA. Ultra-wideband hybrid magneto-electric dielectric-resonator dipole antenna fed by a printed RGW for millimeter-wave applications. IEEE Access. 2022;10:2028-2036

[41] krn5. CST Studio Suite 3D EM Simulation and Analysis Software [Internet]. 2022. Available from: <https://www.3ds.com/products-services/simulia/products/cst-studio-suite/>

[42] Sharifi Sorkherizi M, Kishk Ahmed A. Transition from Microstrip to Printed Ridge Gap Waveguide for Millimeter-Wave Application. Vancouver, BC, Canada: IEEE; 2015. pp. 1588-1589

[43] Pourahmadazar J, Farahani M, Denidni T. Printed Ridge Gap Waveguide Rotman Lens for Millimetre-wave Applications. 2018 18th International Symposium on Antenna Technology and Applied Electromagnetics (ANTEM); 2018. pp. 1-2

[44] Ali MMM. Millimeter-Wave Components and Antennas for Spatial and Polarization Diversity using PRGW Technology [PhD]. Montr'éal, Qu'ebec, Canada: Concordia University; 2020

[45] Ali MMM, Shams SI, Sebak AR. Printed ridge gap waveguide 3-dB coupler: Analysis and design procedure. IEEE Access. 2018;6:8501-8509

[46] Afifi I, Ali MMM, Sebak AR. Analysis and design of a wideband coaxial transition to metal and printed ridge gap waveguide. IEEE Access. 2018; 6:70698-70706

- [47] Han S, Lin IC, Xu Z, Rowell C. Large-scale antenna systems with hybrid analog and digital beamforming for millimeter wave 5G. *IEEE Communications Magazine*. 2015;**53**(1): 186-194
- [48] Ali MMM, Shams SI, Elsaadany M, Sebak A. Printed RGW 3-dB Backward Coupler for Millimeter Wave Applications. In Montreal, QC, Canada: IEEE; 2020
- [49] Ali MMM, Shams SI, Sebak A. Ultra-wideband printed ridge gap waveguide hybrid directional coupler for millimetre wave applications. *IET Microwaves, Antennas & Propagation*. 2019;**13**(8):1181-1187
- [50] MMM A, Denidni TA. A Wideband Millimeter-Wave 3-dB Hybrid Coupler Based on Printed-RGW Technology. Singapore, Singapore: IEEE; 2021
- [51] Afifi I, Sebak AR. Wideband 4×4 butler matrix in the printed ridge gap waveguide technology for millimeter-wave applications. *IEEE Transactions on Antennas and Propagation*. 2020;**68**(11): 7670-7675
- [52] Hildebrand LT. Results for a simple compact narrow-wall directional coupler. *IEEE Microwave and Guided Wave Letters*. 2000;**10**(6):231-232
- [53] Djerafi T, Wu K. Super-compact substrate integrated waveguide cruciform directional coupler. *IEEE Microwave and Wireless Components Letters*. 2007;**17**(11):757-759
- [54] Liu B, Hong W, Zhang Y, Tang HJ, Yin X, Wu K. Half mode substrate integrated waveguide 180° 3-db directional couplers. *IEEE Transactions on Microwave Theory and Techniques*. 2007;**55**(12):2586-2592
- [55] Afifi I, Ali MMM, Sebak AR. Analysis and Design of a 30 GHz Printed Ridge Gap Ring-Crossover. Atlanta, GA, USA: IEEE; 2019. pp. 65-66
- [56] Ali MMM, Afifi I, Sebak AR. Design of Printed RGW Crossover for Millimeter Wave Beam Switching Network. Atlanta, GA, USA: IEEE; 2019. pp. 63-64
- [57] Ali MMM, Sebak A. Compact printed ridge gap waveguide crossover for future 5G wireless communication system. *IEEE Microwave and Wireless Components Letters*. 2018;**28**(7):549-551
- [58] Afifi I. 30 GHz Printed Ridge Gap Components and Antennas for Imaging Systems [PhD]. Montreal, QC, Canada: Concordia University; 2020
- [59] Murai K, Ikeuchi H, Kawai T, Kishihara M, Ohta I. Broadband design method of SIW directional couplers. 2011 China-Japan Joint Microwave Conference; 2011. pp. 1-4
- [60] Zheng SY, Ye XF. Ultra-Compact Wideband Millimeter-Wave Crossover Using Slotted SIW Structure. Nanjing, China: IEEE; 2016. pp. 1-2
- [61] Kutty S, Sen D. Beamforming for millimeter wave communications: An inclusive survey. *IEEE Communications Surveys and Tutorials*. 2016;**18**(2): 949-973
- [62] Afifi I, Sebak AR. Wideband Printed Ridge Gap 45° Schiffman Phase Shifter for Millimeter Wave Systems. Montreal, QC, Canada: IEEE; 2020. pp. 101-102
- [63] Ali MMM, Sebak A. Printed RGW circularly polarized differential feeding antenna array for 5G communications. *IEEE Transactions on Antennas and Propagation*. 2019 May;**67**(5): 3151-3160

- [64] Afifi I, Sebak AR. Wideband printed ridge gap rat-race coupler for differential feeding antenna. *IEEE Access*. 2020;**8**: 78228-78235
- [65] Dehdasht-Heydari R, Forooraghi K, Naser-Moghadasi M. Efficient and accurate analysis of a substrate integrated waveguide (SIW) rat-race coupler excited by four U-shape slot-coupled transitions. *Applied Computational Electromagnetics Society Journal*. 2015 Jan;**1**(30):42-49
- [66] Zou X, Tong CM, Li CZ, Pang WJ. Wideband hybrid ring coupler based on half-mode substrate integrated waveguide. *IEEE Microwave and Wireless Components Letters*. 2014 Sep; **24**(9):596-598
- [67] Ding Y, Wu K. Miniaturized Hybrid Ring Circuits Using T-type Folded Substrate Integrated Waveguide (TFSIW). Boston, MA, USA: IEEE; 2009. pp. 705-708
- [68] Ali AAM, El-Shaarawy HB, Aubert H. Miniaturized hybrid ring coupler using electromagnetic bandgap loaded ridge substrate integrated waveguide. *IEEE Microwave and Wireless Components Letters*. 2011 Sep; **21**(9):471-473
- [69] Afifi I, Alzidani M, Sebak A. Wideband Printed Ridge Gap Waveguide Differential Feeding Aperture Antenna for Millimeter Wave Applications. Atlanta, GA, USA: IEEE; 2019. pp. 267-268
- [70] Ali MMM, Afifi I, Sebak AR. A dual-polarized magneto-electric dipole antenna based on printed ridge gap waveguide technology. *IEEE Transactions on Antennas and Propagation*. 2020 Nov;**68**(11): 7589-7594
- [71] Ali MMM, Sebak AR. 2-D scanning magnetolectric dipole antenna array fed by RGW butler matrix. *IEEE Transactions on Antennas and Propagation*. 2018 Nov;**66**(11):6313-6321
- [72] Afifi I, Ali MMM, Sebak AR. Wideband Printed Ridge Gap Semi-Log Periodic Structure Antenna for Millimeter Wave Applications. 2018 18th International Symposium on Antenna Technology and Applied Electromagnetics (ANTEM); 2018. pp. 1-2